Lasers Med Sci (2007) 22:279–284
DOI 10.1007/s10103-007-0455-9

ORIGINAL ARTICLE

Pulsed photothermal temperature profiling of agar tissue phantoms

Matija Milanič · Boris Majaron · J. Stuart Nelson

Received: 27 October 2006 / Accepted: 20 February 2007 / Published online: 24 May 2007

Abstract We determine experimentally the accuracy of pulsed photothermal radiometric (PPTR) temperature depth profiling in water-based samples. We use custom tissue phantoms composed of agar gel layers separated by very thin absorbing layers. Two configurations of the acquisition system are compared, one using the customary spectral band of the InSb radiation detector (3.0–5.5 μm) and the other with a spectrally narrowed acquisition band (4.5–5.5 μm). The laser-induced temperature depth profiles are reconstructed from measured radiometric signals using a custom minimization algorithm. The results correlate very well with phantom geometry as determined by optical coherence tomography (OCT) and histology in all evaluated samples. Determination of the absorbing layer depth shows good repeatability with spatial resolution decreasing with depth. Spectral filtering improves the accuracy and resolution, especially for shallow absorption layers (~120 μm) and more complex structures (e.g., with two absorbing layers). The average full width at half maximum (FWHM) of the temperature peaks equals 23% of the layer depth.

This work was presented at Laser Florence 2006, Florence, Italy, November 10–11, 2006.

M. Milanič (✉) · B. Majaron
Jožef Stefan Institute,
Jamova 39,
1000 Ljubljana, Slovenia
e-mail: matija.milanic@ijs.si

B. Majaron · J. S. Nelson
Beckman Laser Institute, University of California,
Irvine, CA 92612, USA

J. S. Nelson
Department of Biomedical Engineering, University of California,
Irvine, CA 92612, USA

Keywords Pulsed photothermal radiometry (PPTR) · Optical coherence tomography (OCT) · Imaging techniques · Infrared absorption

Introduction

Success of several laser-based therapeutic procedures depends on the physician's ability to select a suitable combination of treatment parameters on an individual patient basis. In particular, it is believed that knowledge of lesion structure, and possibly, also laser-induced temperature profile, could significantly improve the efficacy and safety of laser therapy of port-wine stain birthmarks (PWS) [1, 2].

Pulsed photothermal radiometry (PPTR) was recognized as a promising technique for non-invasive determination of chromophore distribution in strongly scattering biological tissues and was extensively investigated [3–13]. This technique is based on time-resolved measurement of mid-infrared (IR) emission after pulsed laser irradiation of a sample. When thermal properties are constant throughout the sampled volume, the laser-induced temperature profile can be reconstructed from the radiometric signal. However, numerical simulations and preliminary experimental data suggest that utilizing the entire spectral band of a typical InSb radiation detector may compromise the accuracy of PPTR measurements in biological tissues due to pronounced spectral variation of the absorption coefficient in water between 3 and 4 μm [12, 14, 15].

We present in this paper a systematic experimental comparison of PPTR temperature profiling utilizing the full and appropriately narrowed acquisition spectral band of the InSb detector. All measurements were performed in agar tissue phantoms with subsurface absorbing layers at various depths. A custom algorithm was applied to

reconstruct the initial temperature profiles from the recorded PPTR signals [15]. The chromophore depths determined from these profiles were compared with values determined by optical coherence tomography (OCT) and histology.

Materials and methods

Preparation of tissue phantoms

Our tissue phantoms are composed of agar gel layers with different thickness, separated by very thin absorbing layers (Fig. 1). Agar gel was prepared by dissolving 0.15 mg of agar powder in 6 ml of distilled water. Polymerization was initiated by heating the mixture to the boiling point in a microwave oven. Individual gel layers were produced by pouring the agar solution onto a wetted microscope slide with two identical spacers positioned near the ends of the slide. A second microscope slide was placed on top of the agar solution and gently pressed against the spacers. When polymerization was complete, the top slide was carefully removed, exposing the gel layer of uniform thickness.

The absorbing layers were prepared by powdering the surface of the gel layer with small amounts of fine carbon black powder, which was then covered by another gel layer. Carbon black powder was selected because it is hydrophobic and, therefore, does not diffuse into the agar gel, enabling the preparation of stable thin absorbing layers.

Three tissue phantoms (samples A–C) evaluated in this study, thus, consist of a 1- to 2-mm thick gel substrate, a single absorbing layer, and one superficial gel layer of different thickness (Fig. 1). The depths of their subsurface absorbing layers are ~120, 280, and 450 μm, respectively, which corresponds to the onset of vascular network in shallow, medium, and deep PWS. One tissue phantom (sample D) includes two absorbing layers at approximate depths of 220 and 400 μm. In this sample, we have applied homogeneously dispersed TiO_2 powder to increase optical scattering in the substrate layer. Backscatter from the substrate enhances light fluence in the deeper absorbing layer more than in the upper one, enabling us to produce two comparable temperature peaks despite strong attenuation of the incident laser pulse in the upper absorbing layer [16].

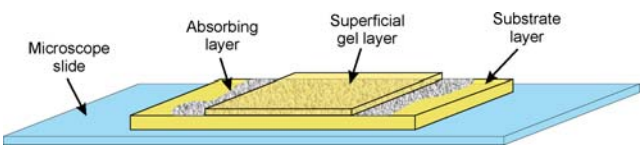

Fig. 1 Schematic of tissue phantoms with a single absorbing layer (samples A–C)

Pulsed photothermal profiling

For each PPTR measurement the sample was irradiated with a single 1.5-ms long 585-nm pulse from a pulsed dye laser (ScleroPlus, Candela, Wayland, MA, USA). Energy density near the center of a 10-mm diameter laser spot was ~3 J/cm^2. The transient increase in IR emission from the central area (1.9×1.9 mm^2) was recorded with an IR camera (Phoenix, Indigo, Santa Barbara, CA, USA) at a rate of 1,083 frames per second. Integration time of the detector was set to 0.5 ms, and the signal acquisition time was 1 s.

We acquired radiometric signals from three different sites on each sample, separated by a few millimeters to prevent thermal interference between successive measurements. On each site, the radiometric signal was acquired both using the full spectral band of the IR camera (3.0–5.5 μm) and with a custom long-pass IR filter (cut-on at 4.5 μm) fitted to the collection optics. PPTR signals were obtained by calibrating the responses of the detector array elements using a computer-controlled black body (BB701, Omega Engineering, Stamford, CT, USA), averaging the temperature measurements across the camera array and subtracting the baseline value.

Derivation of the basic relations of PPTR temperature depth profiling can be found elsewhere [6, 9, 12]. The initial laser-induced temperature profile $\Delta T(z,0)$ can be reconstructed from the transient radiometric signal $\Delta S(t)$ by solving a Fredholm integral equation of the first kind:

$$\Delta S(t) = \int_0^\infty K(z,t)\,\Delta T(z,0)\,dz \tag{1}$$

The kernel function $K(z,t)$ involves thermal properties of the sample material and an effective IR absorption coefficient value for the respective spectral acquisition band, μ_{IR} [12, 16].

Reconstruction of the temperature profile vector $\boldsymbol{T}_{obj}$ from a given PPTR signal $\boldsymbol{S}$ represents a severely ill-posed inverse problem, primarily due to defect rank of the kernel matrix $\boldsymbol{K}$ with elements $K_{i,j}=K(z_j,\ t_i)\ \Delta z$ [6]. Moreover, experimental signals are subject to noise, and matrix $\boldsymbol{K}$ may not describe accurately all the physical processes involved. We, therefore, seek the best approximate solution $\boldsymbol{T}$ by solving the minimization problem:

$$\min\|\boldsymbol{S}-\boldsymbol{K}\cdot\boldsymbol{T}\|^2 \tag{2}$$

We solve the minimization problem using a custom iterative algorithm [15] that combines the minimal-error conjugate gradient scheme [17] with a non-negativity constraint, following the approach of Calvetti et al. [18], and includes adaptive regularization. Elements of the kernel matrix $\boldsymbol{K}$ are calculated using a thermal diffusivity value of 0.13 mm^2/s and μ_{IR}=31.2 mm^{-1}, determined as described

in [19]. The temperature profile, represented by 250 values over a depth range of 2.5 mm, is typically reconstructed in 50–150 iteration steps.

Optical coherence tomography and histology

Several cross-sectional images per sample were acquired using an OCT system with a central source wavelength of 1.3 μm [20]. The axial and lateral scanning lengths were set to 800 μm and 2 mm, respectively. The images were saved in Joint Photographic Experts Group (JPEG) format (400× 634 pixels) for further analysis. For purposes of presentation and analysis, the axial dimensions within the sample were corrected using an estimated index of refraction (1.32). Distance from the sample surface to the center of the absorbing layer was determined at six equidistant positions in each image.

Finally, thin vertical sections were cut from the sample using a pair of blades and placed onto a clean microscope slide. The sections were inspected under a microscope at magnifications of 4, 20, and 40, and photographed using a charge-coupled device (CCD) camera (resolution 552× 744). Depth of the absorbing layer was determined from the microphotographs at ten locations per sample.

Results

Pulsed photothermal radiometric profilometry

PPTR signals acquired from sample A are presented in Fig. 2. The shape of full-spectrum signal (dash line) differs from the spectrally filtered signal (solid line).

Figure 3 presents temperature profiles reconstructed from PPTR measurements on three different sites on sample A, involving the full (3.0–5.5 μm; dash line) and narrowed spectral acquisition bands (4.5–5.5 μm; solid line). With the first approach, peak temperature values are observed at depths of 125, 115, and 105 μm (top to bottom). If we take this as a measure of the absorbing layer depth, it is, thus,

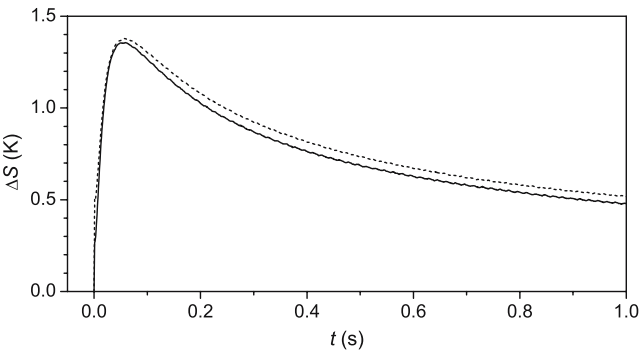

Fig. 2 PPTR signals from sample A acquired with a spectral band of 3.0–5.5 μm (*dash*) and 4.5–5.5 μm (*solid line*)

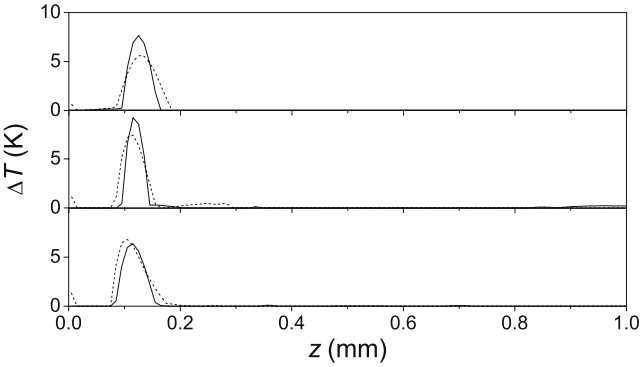

Fig. 3 Temperature profiles at three sites on sample A, reconstructed from PPTR signals acquired using the entire spectral range (3.0–5.5 μm, *dashed line*) and the reduced spectral range (4.5–5 μm, *solid line*)

assessed at 115 μm with a standard deviation of 10 μm. From the measurements with the narrowed spectral band, the absorbing layer depth is 118±6 μm (peak temperature values at 125, 115, and 115 μm).

While the two depths do not differ significantly, it is apparent that the temperature peaks obtained with reduced spectral acquisition are sharper than those reconstructed from PPTR signals using the full spectral bandwidth. The full width at half maximum (FWHM), obtained using spectral filtering, is 30±10 μm, markedly smaller than with non-filtered acquisition (47±6 μm). Moreover, the latter approach consistently results in a small artifact near the sample surface.

Figure 4 presents an analogous set of temperature profiles from sample B. Using the full spectral band (dash lines), the temperature peaks occur at 285 μm in all three sites. With spectrally narrowed acquisition, they are indicated at 265, 265, and 285 μm (solid lines, top to bottom). The temperature profiles are broader than in sample A, and average depths and widths do not differ significantly between the two measurement approaches (see Table 1). In sample C, with the deepest absorbing layer, the temperature profiles are even broader. The average depths and widths obtained with the two acquisition approaches are practically the same (Table 1).

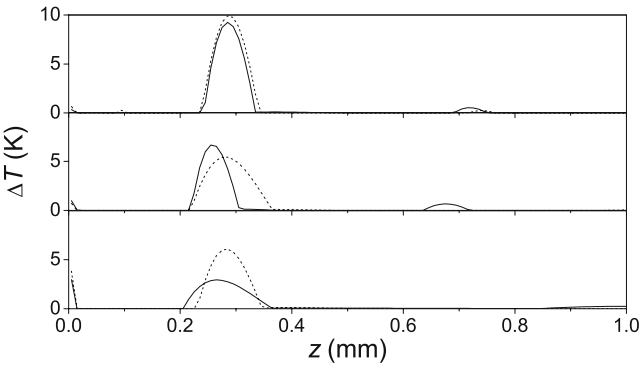

Fig. 4 Temperature profiles at three sites on sample B, reconstructed from PPTR signals acquired using the full spectral range (*dashed line*) and the reduced spectral range (*solid line*)

Table 1 Average depths and widths of the absorbing layers as determined with three measurement techniques

Sample	PPTR, 3–5 μm		PPTR, 4.5–5 μm		OCT		Histology
	Depth	Width	Depth	Width	Depth	Width	
A	115±10	47±6	118±6	30±10	120±15	20	125±15
B	285±0	68±8	272±12	65±22	290±32	20	287±15
C	452±12	138±53	455±10	125±25	472±15	30	450±30
D							
1st peak	218±12	82±8	225±17	42±3	240±3	40	200±4
2nd peak	415±44	176±76	405±36	85±15	412±7	40	340±4

Only depths and standard deviations were determined in case of histology.

Figure 5 presents temperature profiles reconstructed from PPTR measurements on sample D with two subsurface absorbing layers. It is evident that the profiles obtained using the entire acquisition band (dash line) are markedly blurred in comparison with those using the reduced spectral band (solid line). Only the latter approach clearly separates the two layers, which are approximately 0.18 mm apart. The average peak temperature depths and widths for both experimental approaches, together with their standard deviations, are presented in Table 1.

Optical coherence tomography

An OCT cross-sectional image of sample A (Fig. 6a) shows clearly the sample surface (upper arrow) and the absorbing layer (lower arrow) due to strong scattering of incident laser light at these two boundaries. Blurring of both boundary lines that amounts to ~20 μm precludes accurate and reliable determination of the top layer's thickness. If the center of each line is selected to represent the boundary location, the average depth of the absorbing layer is determined as 120 μm with a standard deviation of 15 μm. Sample B (Fig. 6b) displays the largest variation of the top layer thickness, which is determined as 290± 32 μm.

Characteristic "ringing" artifacts are present around the surface line in the image of sample D (Fig. 6c; top arrow). Nevertheless, both absorbing layers are easily discernible (mid- and bottom arrow, respectively), and their average depths are determined at 240 and 412 μm. Pronounced optical scattering due to TiO_2 particles in the gel substrate underneath the deeper absorbing layer is clearly visible in the image. The OCT results from all samples are presented in Table 1.

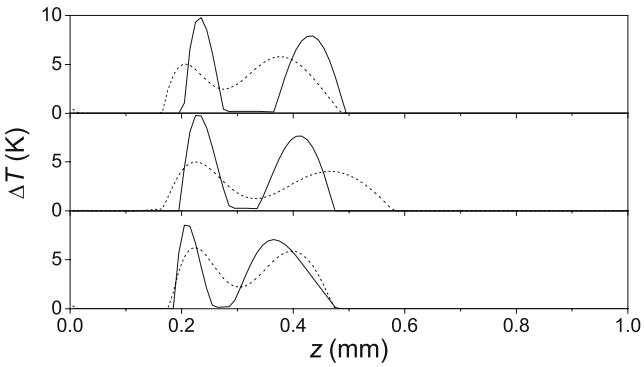

Fig. 5 Temperature profiles at three sites on sample D, reconstructed from PPTR signals acquired using the full spectral range (*dashed line*) and the reduced spectral range (*solid line*)

Histology

Figure 7a presents gross histology of sample C under an optical microscope. Sample surface is indicated by the top arrow. Carbon powder granules are confined to the boundary between the top agar layer and thicker substrate layer (note the 500-μm scale bar). The absorbing layer depth varies with location, resulting in an average value of 450 μm with a standard deviation of 30 μm.

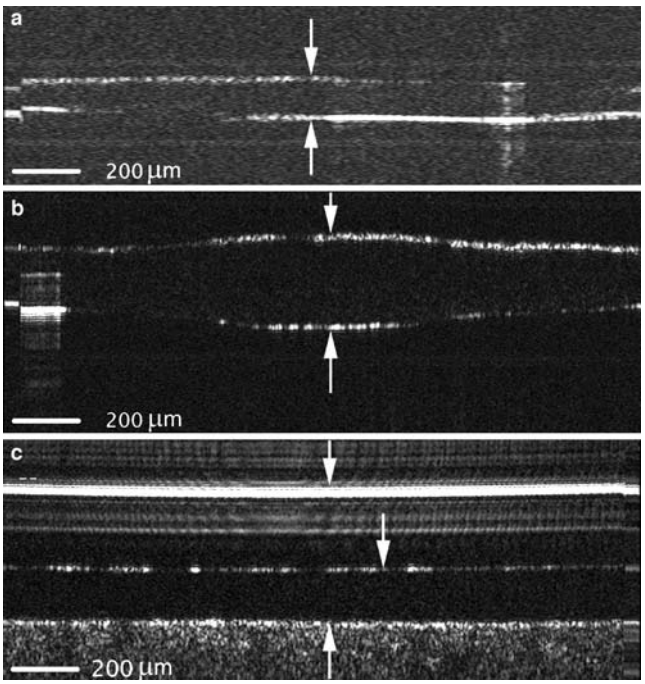

Fig. 6 OCT images of tissue phantoms: **a** sample A and **b** sample B. The *upper arrow* indicates the sample surface, and the *lower* one indicates the absorbing layer. **c** Sample D: The *middle arrow* indicates the first absorbing layer, and the *bottom* one indicates the deeper absorbing layer. The substrate layer (*underneath the latter*) shows scattering due to TiO_2 particles

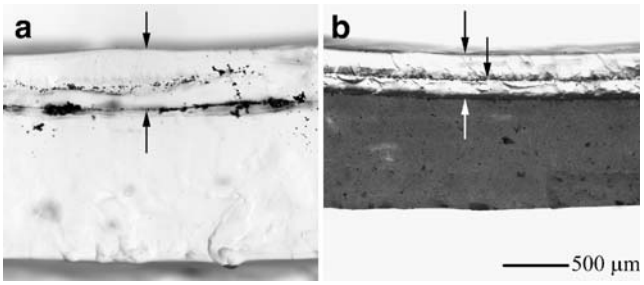

Fig. 7 Gross histology of **a** sample C: The *upper arrow* indicates the sample surface, and the *lower arrow* indicates the absorbing layer. **b** Sample D: The *upper arrow* indicates the sample surface, the *middle arrow* the upper absorbing layer, and the *bottom arrow* the deeper absorbing layer. The substrate layer in sample D appears darker because of pronounced optical scattering (microscope objective, 4×)

Gross histology of sample D is presented in Fig. 7b. The upper arrow indicates the sample surface and the middle arrow the first absorbing layer. The optically scattering substrate layer underneath the second absorbing layer (bottom arrow) appears darker in this transillumination microphotograph. The absorbing layer depths as determined from histology in all samples are presented in Table 1 (last column).

Discussion

The peak temperature depths, determined by PPTR profiling using the entire detection band of the InSb radiation detector and spectrally narrowed signal acquisition, are very similar (see Table 1). In most samples, the difference between the two average values is smaller than their respective standard deviations. In absolute terms, the largest difference is only 13 μm (in sample B). In all other cases, the difference is below the temperature profile discretization (Δz=10 μm).

Nevertheless, appropriate spectral filtering of PPTR signal acquisition improves the reconstructed temperature depth profiles, especially for shallower absorbers. In sample A, the temperature peaks arising from localized absorption at a depth of ~120 μm are rather sharp (Fig. 3, solid lines), with an average FWHM of only 30 μm. The corresponding peaks in full-bandwidth results are significantly broader (47±6 μm; dashed lines) and lower in comparison, just as predicted by numerical simulations [12]. The advantage of spectral filtering is less apparent for deeper absorbing layers (Fig. 4, Table 1), where the temperature profiles obtained with either acquisition approach are increasingly blurred—also in good agreement with earlier reports [9, 10].

In sample D, featuring two absorbing layers (Fig. 5), the average widths of both temperature peaks obtained with spectrally narrowed acquisition are two times smaller than for the full-bandwidth approach (Table 1)—although the second absorption layer is deeper than 400 μm. This reflects the fact that reconstruction of more complex temperature profiles is more susceptible to the deficiency of monochromatic approximation (implicit in the kernel function) used with spectrally broad signal acquisition. By extrapolation, one can predict that in clinical applications of PPTR depth profiling involving even more complex temperature profiles, the benefit of spectral filtering may be even greater than indicated by Fig. 5.

The absorbing layer depths assessed from PPTR depth profiling match the results from OCT and histology within their respective uncertainties. The only discrepancy larger than 5% is found in sample D, where the depths of both layers as determined by histology are 10–15% smaller than those from both PPTR and OCT measurements. The origin of such a discrepancy is most likely shear deformation of the sample during histological sectioning. Besides smearing of carbon granules from the thin absorbing layer (see Fig. 7), artifacts in histological images include also layer separation and folding of the slice. However, these were easy to recognize and such images were excluded from the analysis.

Another potential origin of discrepancies is the shrinking of the gel layers upon evaporation of water from the sample's surface. We tried to minimize this effect by storing the samples at saturated humidity and performing all measurements in rapid succession. However, the samples were inevitably exposed to room conditions during each measurement. Evaporation would have had a particularly strong influence on the thin histological sections illuminated by relatively strong microscope light.

The thickness of the superficial layer in our samples was evidently not truly uniform (see Fig. 6b), and the three measurement techniques were not always applied to exact same locations. Moreover, each histology and OCT image provides information only along a single line, whereas PPTR measurements involve a substantial surface area and, thereby, present an average layer depth within that area. This could explain why standard deviations of absorber depths from PPTR measurements (in samples A–C) are smaller than from histology and OCT.

On the other hand, the same argument suggests that the presented peak widths from PPTR measurements include an unknown contribution due to spatial variation of the superficial layer thickness and, thus, do not reflect the ultimate spatial resolution of the technique. In other words, the peaks could have been narrower than the current 19–28% of the layer depth (average, 23±3%) if the absorbing layer was thinner and the overlying layer had a perfectly uniform thickness.

With both PPTR acquisition approaches, $\mu_{IR}(\lambda)$ varies within the spectral acquisition band, raising a legitimate question about the optimal effective value to use in the reconstruction process based on monochromatic approxi-

mation (Eq. 1). The value used in the present analysis is based on a systematic study [19], which will be described in a separate publication.

We have added the TiO_2 powder to the substrate layer of sample D to achieve similar temperature rises in both absorbing layers and, thereby, enable a fair analysis of PPTR profiling performance. Without this provision, the temperature rise in the deeper absorbing layer was 3–5 times lower than in the upper one due to strong attenuation of the incident laser beam in the latter. The resulting increase in optical scattering is reflected both in enhanced OCT signal (Fig. 6d) and in dark appearance of the layer in transillumination microphotograph (Fig. 7b).

Note, however, that we analyze the accuracy of PPTR temperature profiling, without intent to determine the samples' optical properties. To that end, the genesis of test temperature profiles is entirely irrelevant, and optical scattering of the samples (in the visible) does not have to resemble that of human skin to ensure that the results are transferable to PPTR temperature profiling in vivo. What matters is that both materials have similar absorption properties in the acquisition spectral range and that scattering in that range is negligible in comparison [21, 22].

Conclusions

Depths of thin absorbing layers as determined by PPTR temperature profiling are in very good agreement with those determined by OCT and histology. Temperature profiles reconstructed from PPTR signals with reduced spectral bandwidth feature sharper temperature peaks than with full-bandwidth acquisition. The advantage of the former is particularly apparent in shallow and/or more complex absorbing structures. PPTR temperature profiling utilizing the 4.5- to 5.5-μm detection band, therefore, enables more accurate determination of subsurface chromophore distribution.

Acknowledgment The authors thank Prof. Bernard Choi for help with PPTR instrumentation, Dr. Jeehyun Kim for assistance with OCT imaging, and Lih-Huei L. Liaw, MS, for expertise regarding histology. This project was supported by the Slovenian Research Agency, National Institutes of Health (AR47551 and AR48458), and Beckman Laser Institute institutional support.

References

1. van Gemert MJC, Nelson JS, Milner TE, Smithies DJ, Verkruysse W, de Boer JF, Lucassen GW, Goodman DM, Tanenbaum BS, Norvang LT, Svaasand LO (1997) Non-invasive determination of port wine stain anatomy and physiology for optimal laser treatment strategies. Phys Med Biol 42:937–950
2. Verkruysse W, Majaron B, Tanenbaum BS, Nelson JS (2000) Optimal cryogen spray cooling parameters for pulsed laser treatment of port wine stains. Lasers Surg Med 27:165–170
3. Long FH, Anderson RR, Deutch TF (1987) Pulsed photothermal radiometry for depth profiling of layered media. Appl Phys Lett 51:2076–2078
4. Jacques SL, Nelson JS, Wright WH, Milner TE (1993) Pulsed photothermal radiometry of portwine-stain lesions. Appl Opt 32:2439–2446
5. Bindra RMS, Imhof RE, Eccleston GM (1994) In vivo opto-thermal measurement of epidermal thickness. J Phys IV C7:445–448
6. Milner TE, Goodman DM, Tanenbaum BS, Nelson JS (1995) Depth profiling of laser-heated chromophores in biological tissues by pulsed photothermal radiometry. J Opt Soc Am A 12:1479–1488
7. Vitkin IA, Wilson BC, Anderson RR (1995) Analysis of layered scattering materials by pulsed photothermal radiometry-application to photon propagation in tissue. Appl Opt 34:2973–2982
8. Milner TE, Smithies DJ, Goodman DM, Lau A, Nelson JS (1996) Depth determination of chromophores in human skin by pulsed photothermal radiometry. Appl Opt 35:3379–3385
9. Sathyam US, Prahl SA (1997) Limitations in measurement of subsurface temperatures using pulsed photothermal radiometry. J Biomed Opt 2:251–261
10. Smithies DJ, Milner TE, Tanenbaum BS, Goodman DM, Nelson JS (1998) Accuracy of subsurface distributions computed from pulsed photothermal radiometry. Phys Med Biol 43:2453–2463
11. Majaron B, Verkruysse W, Tanenbaum BS, Milner TE, Telenkov SA, Goodman DM, Nelson JS (2000) Combining two excitation wavelengths for pulsed photothermal profiling of hypervascular lesions in human skin. Phys Med Biol 45:1913–1922
12. Majaron B, Verkruysse W, Tanenbaum BS, Milner TE, Nelson JS (2002) Spectral variation of infrared absorption coefficient in pulsed photothermal profiling of biological samples. Phys Med Biol 47:1929–1946
13. Choi B, Majaron B, Nelson JS (2004) Computational model to evaluate port wine stain depth profiling using pulsed photothermal radiometry. J Biomed Opt 9:299–307
14. Majaron B, Milanič M, Choi B, Nelson JS (2004) Selection of optimal infrared detector for pulsed photothermal profiling of vascular lesions. Proc SPIE 5318:121–132
15. Majaron B, Milanič M (2007) Re-evaluation of pulsed photothermal radiometric profiling in samples with spectrally varied infrared absorption coefficient. Phys Med Biol 52:1089–1101
16. Wilson BC (1995) Measurement of tissue optical properties: methods and theories. In: Welch JA (ed) Optical-thermal response of laser-irradiated tissue. Plenum, New York, pp 233–271
17. Hanke M (1995) Conjugate gradient type method for Ill-posed problems. Longman Scientific & Technical, Harlow
18. Calvetti D, Landi G, Reichel L, Sagallari F (2004) Non-negativity and iterative methods for ill-posed problems. Inverse Probl 20:1747–1758
19. Majaron B, Milanič M (2006) Effective infrared absorption coefficient for photothermal radiometric measurements in biological tissues. Lasers Surg Med Suppl 18:4
20. Kim J, Oh J, Milner TE, Nelson JS (2006) Hemoglobin contrast in magnetomotive optical Doppler tomography. Opt Lett 6:778–780
21. Vitkin IA, Wilson BC, Anderson RR, Prahl SA (1994) Pulsed photothermal radiometry in optically transparent media containing discrete optical absorbers. Phys Med Biol 39:1721–1744
22. Viator JA, Choi B, Peavy GM, Kimel S, Nelson JS (2003) Spectra from 2.5–15 μm of tissue phantom materials, optical clearing agents and ex vivo human skin: implications for depth profiling of human skin. Phys Med Biol 48:N15–N24